3D Printing of Continuous Fiber Composites Using Two-stage UV Curable Resin

Huan Jiang[1], Arif M. Abdullah [1], Yuchen Ding [1], Christopher Chung [1], Martin Dunn [1, *], Kai Yu [1, *]

[1] Department of Mechanical Engineering, University of Colorado Denver, Denver, CO 80217, United States of America

[*] Corresponding author MD: martin.dunn@ucdenver.edu, KY: kai.2.yu@ucdenver.edu

Abstract: 3D printing allows for moldless fabrication of continuous fiber composites with high design freedom and low manufacturing cost per part, which makes it particularly well-suited for rapid prototyping and composite product development. Compared to thermal-curable resins, UV-curable resins enable the 3D printing of composites with high fiber content and faster manufacturing speeds. However, the printed composites exhibit low mechanical strength and weak interfacial bonding for high-performance engineering applications. In addition, they are typically not reprocessable or repairable; If they could, it would dramatically benefit the rapid prototyping of composite products with improved durability, reliability, cost savings, and streamlined workflow. In this study, we demonstrate that the recently emerged two-stage UV-curable resin is an ideal material candidate to tackle these grand challenges in 3D printing of thermoset composites with continuous carbon fiber. The resin consists primarily of acrylate monomers and crosslinkers with exchangeable covalent bonds. During the printing process, composite filaments containing up to 30.9% carbon fiber can be rapidly deposited and solidified through UV irradiation. After printing, the printed composites are subjected to post-heating. Their mechanical stiffness, strength, and inter-filament bonding are significantly enhanced due to the bond exchange reactions within the thermoset matrix. Furthermore, the utilization of the two-stage curable resin enables the repair, reshaping, and recycling of 3D printed thermosetting composites. This study represents the first detailed study to explore the benefits of using two-stage UV curable resins for composite printing. The fundamental understanding could potentially be extended to other types of two-stage curable resins with different molecular mechanisms.

Keywords: Direct ink writing; 3D printing; Two-stage UV-curable thermosets; Continuous fiber composites

1. Introduction

Polymer composites with a superior combination of high stiffness, strength, and lightweight properties are in high demand across various applications [1, 2]. Different 3D printing methods have been developed for rapid prototyping and composite product development. For example, 3D printing of composites with nanoparticles (e.g. carbon black, carbon nanotubes) and short fibers was demonstrated using stereolithography [3, 4], digital light processing (DLP) [5, 6], and inkjet methods [7, 8]. However, the direct incorporation of continuous fiber into these printing processes presents a significant challenge. Currently, 3D printing of continuous fiber-reinforced polymer composites (CFRPs) primarily relies on extrusion-based methods, such as fused deposition modeling (FDM) [9-20], in which filament and continuous fibers were supplied separately to the printer head. This process is limited to printing thermoplastic composites, which typically do not possess the required stiffness and strength required for high-performance applications.

Alternatively, thermoset composites with continuous fibers offer outstanding mechanical performance, thermal stability, and chemical resistance due to their crosslinked matrix materials [21]. The 3D printing methods for these composites can be categorized based on the chemical nature of the matrix resins, either thermally curable or UV-curable. For thermally curable composites, Fang et al. [22] and Ming et al. [23] demonstrated the 3D printing of epoxy composites with continuous carbon fiber. Due to the high molecular weight, the epoxy resin remained in a nearly solid state at room temperature and therefore can be printed in a process similar to the FDM. Subsequently, He et al. [24] introduced a design of a 3D printer head based on the direct-ink-writing (DIW) method. It utilized shear stress imposed on the fiber to drive filament deposition and could be employed to print various thermosetting resins with different viscosities. Despite recent advancements, 3D printing of thermally curable composites typically imposes strict requirements on the rheological properties of printable inks; since the matrix is essentially viscous liquid right after the filament deposition, and its ability to print complex geometries is limited.

To achieve a higher fiber content and rapid manufacturing of CFRPs, UV-curable resins [25, 26] are preferred. During the printing, the matrix materials solidify rapidly upon UV irradiation, allowing for the deposition of composite filaments with a high fiber content as the nozzle moves forward. Additionally, UV-curable resins enable the free-standing 3D printing of complex composite structures with minimal need for supporting materials. However, the mechanical strength of printed UV-curable composites is often insufficient for high-level engineering

applications [27, 28]. The composite filaments and printing layers are primarily connected by non-covalent Van der Waals interactions, which leads to a weak interfacial bonding strength [29-32]. Additionally, UV-curable resins face challenges when printing composites with a high carbon fiber content. The presence of carbon fiber significantly blocks light penetration, leading to non-uniform curing of the matrix materials during printing.

Another grand challenge in the field of composite 3D printing is that the printed thermoset composites are not reprocessable and repairable due to their permanently crosslinked matrix [33]. If they could, it would dramatically enhance the durability and reliability of composite prototypes, reduce the time and effort required for frequent remanufacturing caused by minor damages, and enable faster feedback loops between designers and engineers to accelerate the design iteration cycle. In addition, the non-recyclable nature of thermoset composites, coupled with the rapid growth of 3D printing, is leading to an increase in composite waste being generated and released into the environment [34-38]. As a result, there is a pressing need for sustainable 3D printing of recyclable composites to minimize the manufacturing cost and mitigate the generation of hazard waste. Several research studies have been conducted to develop reprocessable and recyclable composites utilizing different mechanisms [39-44]. These composites incorporate dynamic reversible bonds, which not only enhance their recyclability but also enable reversible crosslinking between fibers and the polymer matrix, resulting in significantly improved mechanical properties [40]. Furthermore, the use of bio-based feedstock materials holds the potential for sustainable composite manufacturing, reducing the generation of hazardous waste. However, the direct integration of these innovative material systems with composite 3D printing remains largely unexplored.

Recent materials innovations in two-stage UV curable resin [45-50] offer exciting opportunities to tackle the abovementioned challenges in the 3D printing of thermoset CFRPs. A two-stage UV-curable resin typically consists of acrylate mixtures, allowing for rapid curing upon UV irradiation (the first-stage polymerization). Subsequently, the materials will be subject to post-heating, wherein the covalent reactions dramatically increase the material's crosslinking density and mechanical strength (the second-stage polymerization). This stiffening effect is achieved through covalent reactions among excess chemical bonds or through the recently emerged bond exchange reactions (BERs) [43, 46, 51-57]. Since the second-stage polymerization is thermally triggered, it can enable unform curing of the matrix resin during the composite manufacturing. Another advantage of employing two-stage UV-curable resins for printing is the significant enhancement of bonding

strength between printing filaments and layers, as the dynamic BERs during the post-heating lead to chain connections on the interface through covalent bonding. Additionally, this approach offers significant opportunities for reshaping, repairing, and recycling 3D printed composites. To date, a wide variety of two-stage UV-curable resins have been developed and are commercially available. However, as far as we know, there is no existing work to explore their effectiveness and benefits in enhancing the mechanical properties of 3D printed CFRPs.

In this paper, an acrylate-based two-stage UV curable resin was adopted to 3D print CFRPs using the DIW method [58-62]. The resin was prepared by mixing an acrylate monomer, crosslinker, and photo initiator for UV polymerization. Triazabicyclodecene was added as the catalyst to accelerate the transesterification BERs. Upon UV-irradiation, the free-radical polymerization among acrylate groups formed a loosely crosslinked network. During the subsequent post-heating process, transesterification BERs between ester and hydroxyl groups facilitated the creation of additional crosslinking sites within the network. This substantially increased the crosslinking density and mechanical properties of the composite. The mechanical behaviors of the DIW printed composites with different fiber contents were extensively examined before and after heat treatment. The results demonstrated significant enhancement in mechanical properties compared to UV-curable composites prior to the second-stage polymerization. In addition, due to the malleable matrix enabled by BERs at high temperature, the printed composite lamina can be readily reshaped into 3D configurations through simple thermal processing, which avoids the need for expensive molds or complicated pathway planning to 3D print complex structures [63-66]. The printed composites also exhibit excellent repairability and recyclability. This study represents the first to explore the benefits of using two-stage UV curable resin for composite printing. The fundamental understanding can be potentially extended to other types of two-stage curable resins with different molecular mechanisms.

2. Results and Discussion

2.1 Properties of the two-stage UV curable resin

The UV-curable resin was prepared using the monomer 2-hydroxy-3-phenoxypropyl acrylate, the crosslinker biphenol A glycerolate diacrylate, the photo initiator phenylbis (2,4,6-trimethylbenzoyl) phosphine oxide, and the BER catalyst triazabicyclodecene. The chemical structures of these ingredients are illustrated in **Figure 1a**. The polymerization process of the UV-

curable resin involves two stages. In Stage 1, the acrylate functional groups within the resin mixture undergo free-radical polymerization when exposed to UV light. This process involves opening the double bonds, resulting in the formation of a loosely crosslinked network (represented by black dots in **Figure 1b**) with mechanically effective polymer chains. In the **Supplementary Material** (Section S1, **Figure S1**), a schematic view of the network chemical structures is presented to highlight the working mechanisms of the thermal treatment. The detailed chemical structure of the crosslinking sites before thermal treatment is shown in **Figure S1d.** In addition to mechanically effective chains, in the untreated network, the mono-acrylate HPDDA monomers with one end attached to the polymer network (green chains in the figures) are considered as dangling chains. For clarity, **Figure 1b** shows only five dangling chains, but in the actual polymer network, taking into account the mole ratio between cross-linker and monomer, there are an average of nine dangling chains between two crosslinking sites. In Stage 2, the network is subjected to heat treatment, which triggers transesterification reactions between the hydroxyl and ester groups. The network structure is illustrated in **Figure 1c**. The transesterification BERs between dangling chains and polymer network add new crosslinking sites in the system (represented by red dots in **Figure 1c**). Detailed chemical structure of the additional crosslinking sites is shown in **Figure S1e.** The new crosslinking sites dramatically increase the overall crosslinking density, and therefore change the thermomechanical properties of printed samples. In addition, BERs also generate isolated chain segments (**Figure S1f**), which might be involved in another BER and connected to the network structures again

Fourier Transform Infrared (FTIR) spectrum was performed on the cured resin both before and after heat treatment, and the corresponding results are depicted in **Figure 1d** and **Figure 1e**. Our observations reveal that the relative absorbance of major chemical groups, such as ester and hydroxyl, remains almost constant after heat treatment at 160oC for different times. This consistent pattern suggests that the heat treatment process does not lead to the formation of new chemical compounds. Instead, it involves the exchange of esters and hydroxyl groups during transesterification. Similar findings have been reported in a previous study conducted by Zhang et al. [67] **Figure 1f** compares the glass transition behaviors of the UV cured resin before and after heat treatment. Each curve exhibited only a single narrow peak of tan δ, indicating a homogeneous polymer network without phase-separated structures or domains with different viscoelastic properties [68]. After heat treatment at 160 °C for one hour, the T_g increases from 36.6 °C to 56.3 °C.

The polymer was transformed from a compliant solid at room temperature to a load-bearing stiff material [67]. Simultaneously, the rubbery modulus at temperature well above the T_g increases from 7.69 MPa to 11.22 MPa, indicating a notable increase in network crosslinking density due to the BERs.

In order to assess the mechanical properties of the cured resin before and after the heat treatment, tensile experiments were conducted, and the results are shown in **Figure 1g** and **Figure 1h**. The specimens were subjected to different temperatures of 100 °C, 120 °C, 140 °C, 160 °C, and 180 °C during the one-hour treatment. The engineering stress-strain curves are compared in **Figure 1g**. It is observed that both the material stiffness and strength increase with the temperature of heat treatment. In addition, the duration of the heat treatment also affects the final mechanical properties. As revealed in the previous study [46], the evolution of material stiffness follows an Arrhenius-type time-temperature superposition principle.

After heat treatment at 160 °C for one hour, the stiffness of the cured resin significantly increases by ~11 times compared to the untreated sample (from 169 MPa to 2.14 GPa), and the strength is increased by ~23 times (from 2.1 MPa to 52.2 MPa). The adopted two-stage UV-curable resin exhibits outstanding mechanical properties that are comparable to those of engineering epoxy, which can serve as an ideal matrix material for the 3D printing of high-performance thermoset composites. It is also observed that the mechanical properties of the matrix materials are significantly improved between100 ˚C and 160˚C. However, as the temperature further increased to 180˚C, the stiffness and strength slightly dropped, which could be attributed to the thermal degradation of the polymeric materials after long-time heating. The characterization results indicate that after heating at 160˚C for one hour, the crosslinking density of the matrix materials reaches its peak value with a near-complete stiffening effect of BERs. Therefore, all heat treatments of the 3D printed CFRPs were set at 160 °C to achieve optimal mechanical performance. This experimental method can serve as a general method to establish thermal treatment parameters when working with different types of two-stage resins. Of course, the same thermal treatment parameters can be identified by maintaining a constant heating temperature and varying the heating time. However, the identification process of optimal treatment parameters may be less efficient.

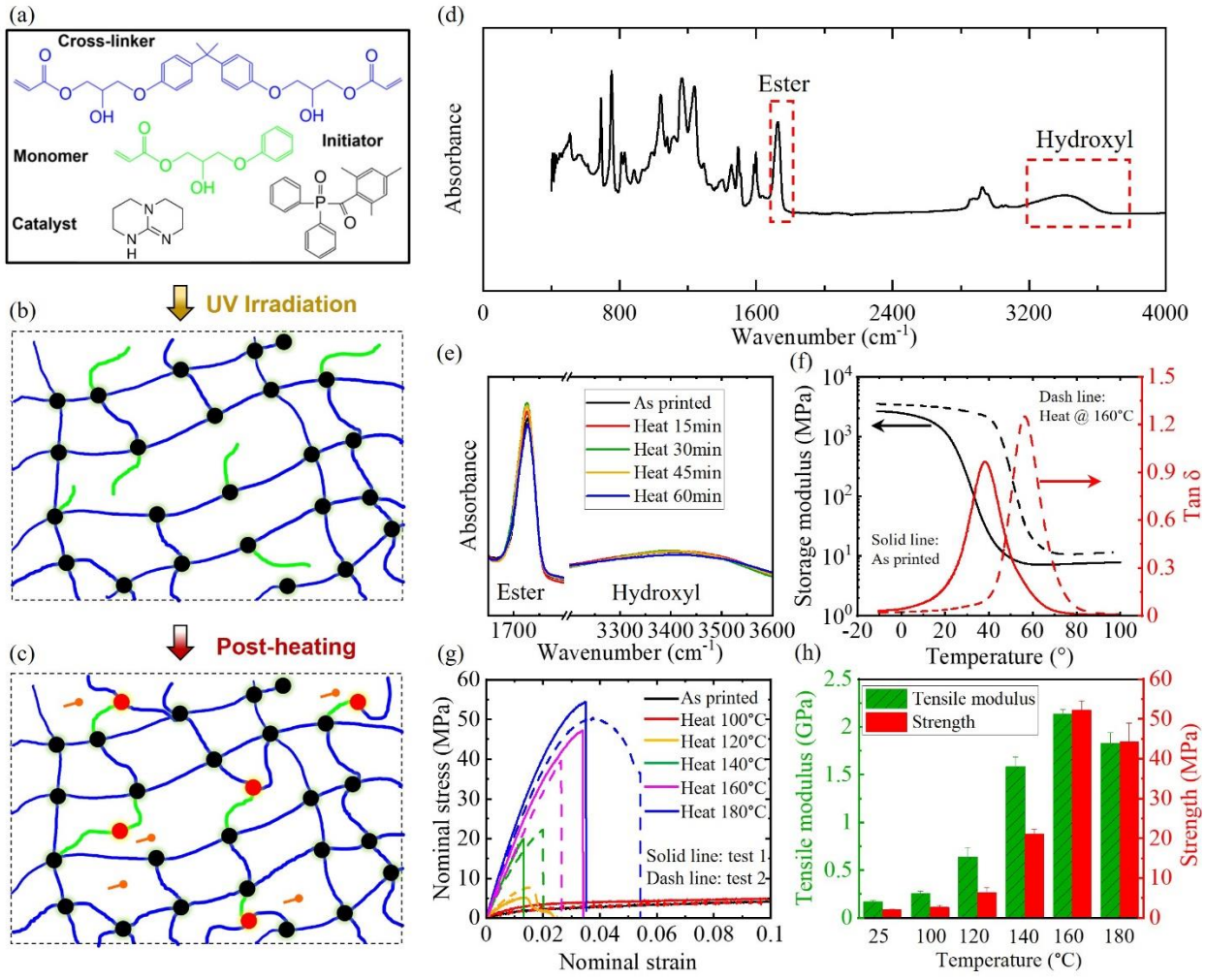

Figure 1. Two-stage UV-curable resin and its properties before and after heat treatment. (a) Chemical structures of monomer, crosslinker, photo initiator, and catalyst in the solution. (b) The first-stage UV curing forms loosely crosslinked network (black dots). (c) The second-stage heat treatment triggers transesterification BERs and form additional crosslinking sites (red dots). (d) FTIR spectrum of the cured resin after being heated for different times. (e) Zoom-in view of the absorption peaks for ester and hydroxyl groups. (f) The storage modulus and tan δ of the cured resin before and after post-heating at 160 ºC for one hour. (g) Nominal stress-strain curves of the cured resin before and after being heated at 100 ˚C, 120 ˚C, 140 ˚C, 160 ˚C, and 180 ˚C, respectively, for an hour. Solid and dashed lines represent two tensile tests on the same type of sample. (h) A summary plot of tensile modulus and strength of the cured resin before and after being heated at 100 ˚C, 120 ˚C, 140 ˚C, 160 ˚C, and 180 ˚C, respectively, for an hour.

2.2 Mechanical properties of 3D printed CFRPs

The adopted DIW setup for the 3D printing of CFRPs is schematically shown in the **Supplementary Materials, Figure S2**. The mechanical performance of 3D printed CFRPs before and after heat treatment was examined with different fiber volume fractions. Composite filaments, lamina, and laminates were printed using the 1k fiber bundle (CST the Composites Store Inc. Tehachapi, CA, USA) and then characterized through room-temperature uniaxial tension tests and three-point bending tests.

The interfacial bonding between the fiber bundle and polymer matrix has a significant impact on the mechanical properties of fabricated composites. Several studies have explored strategies to enhance this bonding through chemical treatments of fibers, thereby improving the surface adhesion with the matrix material. For example, Zhao et al. [69] successfully improved the interfacial bonding between fiber and polymer resin by grafting carbon nanotubes onto the fiber surface. Zhang et al. [70] also reported enhanced bonding strength in composites by directly grafting amino-functionalized graphene oxide onto the carbon fiber surface. In this study, our primary focus is to investigate the benefits of the two-stage curable resin. Therefore, we chose to not perform any surface treatment to the fiber bundle during all our experimental characterization to establish a consistent comparison. Nevertheless, it is important to acknowledge that the fiber/matrix interfaces and the mechanical properties of printed composites have the potential for further improvement through suitable fiber surface treatments, which deserve our future rigorous study.

In our prior work [26], the fiber volume fraction of 3D printed CFRPs was shown to be affected by several material and printing parameters, including resin viscosity, deposition needle diameter, filament spacing, and nozzle moving speed. Specifically, we observed that the fiber content increases with higher resin viscosity, a slower nozzle moving speed, or the use of a deposition needle with a smaller inner diameter. In such cases, less resin adheres to the fiber bundle after filament deposition, resulting in a higher fiber content. Additionally, reducing the spacing between adjacent filaments led to an increase in fiber content. In this current study, our primary focus is on the advantages of employing a two-stage resin as the composite matrix material. To maintain consistency, all influencing parameters are kept the same, with a 0.5 mm filament spacing and a 1 mm/s printing speed. The fiber volume fraction is controlled by using nozzles in different diameters, ranging from Gauge 21 to Gauge 15, with inner diameters spanning from 0.51 mm to 1.36 mm. The measurements of the fiber volume fraction were based on the density of the

composites and the matrix polymers. More detailed information can be found in the **Supplementary Materials** (Section S3).

Mechanical properties of composite filaments

Composite filaments were printed using five different nozzles of varying sizes. Their fiber volume fractions were determined to be 7.1%, 10.7%, 14.8%, 21.6%, and 30.9%, respectively. **Figure 2a** shows the images of three selected filaments with their width indicated by red dashed lines. When using a larger deposition nozzle, there will be more resin attached to the fiber bundle, leading to a lower fiber volume fraction of the composite filament. **Figure 2b** and **Figure 2c** show the nominal stress-strain relationship of filaments with different fiber volume fractions before and after heat treatment. The Young's moduli of the filaments (within the 0.2% initial strain) are summarized in **Figure 2d**. Additionally, the filament modulus was predicted using the rule of mixture (ROM) and presented in the figure for comparison. Note that the modulus of the dry fiber bundle was determined to be 174 GPa through uniaxial tension tests, as described in the **Supplementary Material** (Section S4).

The figures provide interesting insights into the mechanical properties of the filaments. First, with the increment of the fiber volume fraction, the filaments improved enhanced mechanical properties in terms of Young's modulus and ultimate strength. At relatively low fiber contents, the modulus closely aligns with the predictions from ROM. However, at higher fiber contents, notable deviations from the ROM predictions can be observed. For example, when V_f=30.9%, the ROM predicted Young's modulus is 53.8 GPa, whereas the tested modulus of the filaments before heat treatment is 39.9 GPa, representing a 25.8% difference. Second, it is intriguing to observe that the filament modulus notably increases after heat treatment, particularly for filaments with higher fiber volume fractions. This finding contradicts the conventional understanding of composites, where the longitudinal modulus is typically governed by the fiber volume fraction, while the influence of the matrix properties is presumed to be minimal.

These observations in mechanical properties can be attributed to the manufacturing defects that arise during the 3D printing process. With a high fiber volume fraction, the carbon fiber can significantly block the penetration of UV light, leading to nonuniform curing of the matrix resin. This nonuniform curing introduces inhomogeneities in the structure of the filaments, compromising their structural integrity and the efficiency of load transfer between the fiber and

matrix. Furthermore, the inherent stiffness of the carbon fiber causes the continuous bundle to exhibit slight curvature within the composite filament, especially when the matrix resin is insufficiently cured to secure the fibers. Similar observations of the fiber bundle curvature have been reported in other studies on composite 3D printing [71, 72]. These two interrelated mechanisms contribute to a lower stiffness of the composite filaments than the theoretically predicted ROM values. After heat treatment, the matrix stiffness is substantially enhanced, which assists in holding the fiber and improves the bonding strength at the fiber/matrix interface. As a result, the composite modulus is improved and approaches the ROM predictions more closely. The results highlight the importance of using two-stage UV curable resin when printing composites with higher fiber content.

Mechanical property of composite lamina along longitudinal and transverse directions

Composite lamina samples were 3D printed with three different fiber volume fractions (7.1%, 14.8%, and 30.9%). **Figure 2e** shows a printed square lamina sample containing 14.8% carbon fiber as a demonstration. Subsequently, the printed composite samples were precisely cut into a specific geometry tailored for uniaxial tension tests. Details regarding the samples' configuration and dimensions can be found in the **Supplementary Materials** (Section S4).

Figure 2f and **Figure 2g** show the nominal stress-strain relationships in the longitudinal direction before and after the heat treatment. Similar to the behaviors observed in single filaments, the second-stage heat treatment enhances the lamina stiffness, particularly for those with a high fiber content. Furthermore, the composites exhibit improved ultimate strength while maintaining the same level of failure strain at around 1%. The corresponding ultimate strength and fracture toughness, represented by the area under the stress-strain curve, are summarized in **Figure 2h**. After heat treatment, the enhanced stiffness of the matrix contributes to the improved structural integrity of the composite system and efficiency of load transfer at the fiber/matrix interface. Specifically, the composite lamina with 30.9% fiber experiences the most significant increase in both ultimate strength (by 25.3%, from 292.6 MPa to 366.5 MPa) and fracture energy (by 17.3%, from 1.28 MJ/m^3 to 1.50 MJ/m^3) after the heat treatment.

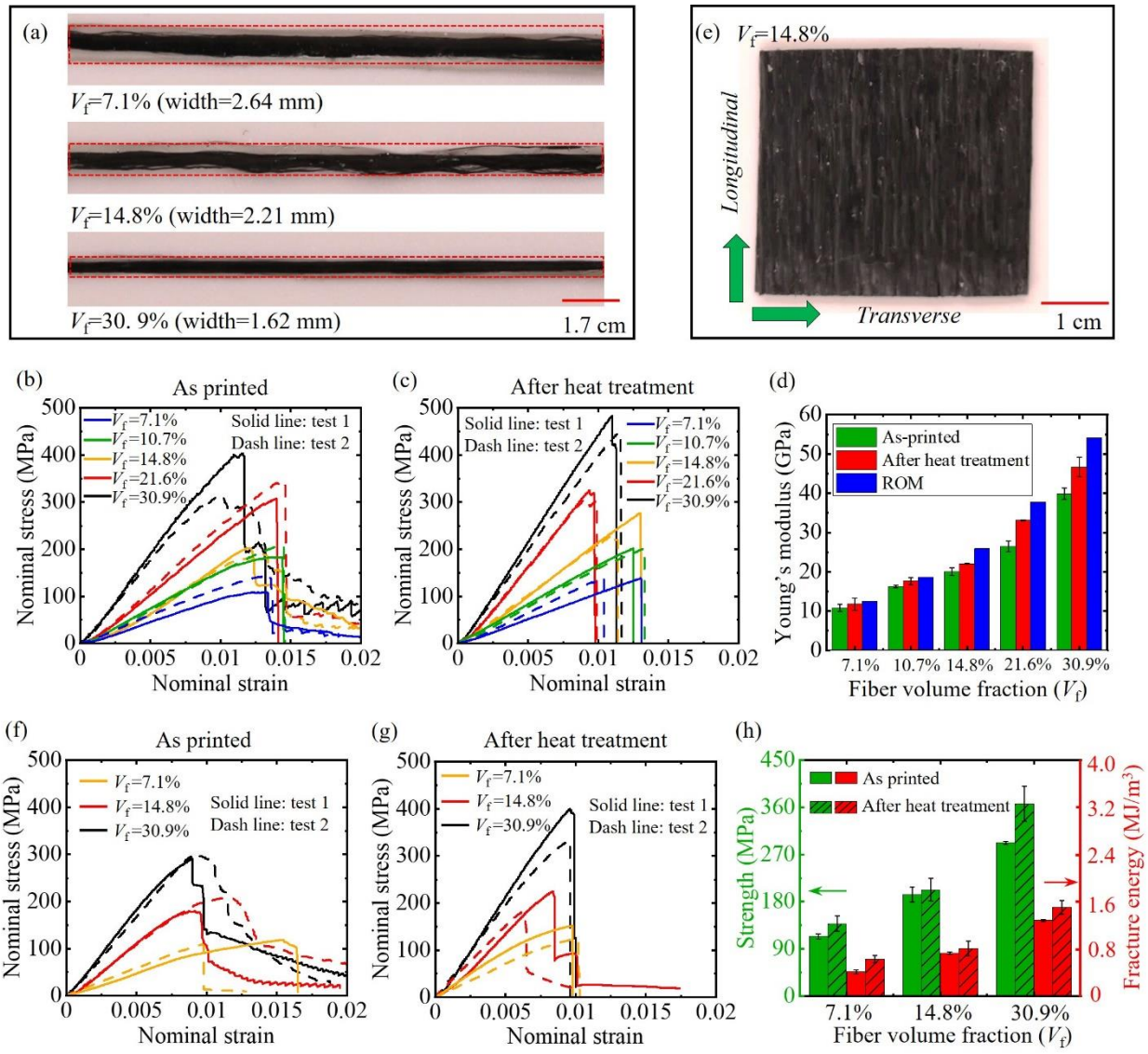

Figure 2. Mechanical performance of composite filaments and lamina along the fiber direction before and after the heat treatment. (a) Filament samples with different fiber volume fractions. The highlighted region indicates the boundary of filaments. (b)- (c) Nominal stress-strain for the filaments with different fiber volume fractions before and after heat treatment. (d) A summary of the Young's modulus for the filaments with different volume fractions. (e) Lamina samples with different fiber volume fractions. (f)-(g) Nominal stress-strain for the lamina samples with different fiber volume fractions before and after heat treatment. (h) A summary of the strength and fracture energy of the lamina samples with different volume fractions.

The weak bonding strength between adjacent filaments and printing layers has been a long-standing challenge in the field of 3D printing of polymers and composites. Herein, we examine how the adoption of a two-stage UV curable resin can enhance the bonding strength of composite

lamina in the transverse direction. The composite lamina samples were 3D printed with different fiber volume fractions (14.8% and 30.9%). The nominal stress-strain curves, ultimate strength, and fracture energy before and after the heat treatment are shown in **Figure 3a, Figure 3b,** and **Figure 3c**.

First, it is observed that the transverse bonding strength of composite lamina with a higher fiber volume fraction is significantly lower than the one with a lower fiber volume fraction. Similar findings have been reported in previous studies [26, 34]. This disparity can be resulted from the insufficient amount of resin around the filament that leads to weak bonding between the composite filaments. Second, after the second-stage heat treatment, the composite lamina shows a lower failure strain (indicated by the strain at notable damage) compared to the lamina without heat treatment. The transverse bonding strength of both lamina samples is substantially enhanced. The ultimate strength increases by 101% and 141% for fiber volume fraction of 30.9% and 14.8% respectively, when compared to the lamina without heat treatment. The fracture energy is increased by 103% and 73%. This is attributed to the covalent bonding and interface welding effect of the adopted two-stage resin. During the heat treatment, the network BERs will not only enhance the bulk stiffness, but also lead to the polymer chains gradually connected on the filament interface through covalent bonding. This covalent bonding enables significantly higher bonding strength compared to systems that rely solely on weak non-covalent interactions between the composite filaments.

As revealed in previous studies [42, 73, 74], with a sufficient amount of heating time, the ultimate strength of welded polymers with BERs is expected to reach the same level as undamaged materials. However, our experimental results show that after heat treatment, the transverse strength of the lamina with 30.9% fiber remains lower than that with 14.8% fiber. This could result from the interfacial defects among composite filaments, such as voids formation, which cannot be completely closed by themselves during the heat treatment. To address this issue, it is suggested that applying proper pressure during the printing process would be beneficial in closing the voids within the printed composites and further enhancing the bonding strength.

Mechanical properties of composite laminate

0/90˚ symmetric laminate samples were 3D printed with 14.8% carbon fiber to evaluate their mechanical performance. The samples were printed with four layers. Within each layer, the

composite filaments are deposited with a ~2mm gap, resulting in a lattice-like structure as the final sample. All samples were subsequently trimmed to the uniform dimension of 13.5mm in width, 110mm in length, and 2.2mm in thickness. **Figure 3d** compares the sample appearances before and after the heat treatment at 160°C for one hour. The printed composites exhibit good thermal stability without shape distortion. Their mechanical properties were characterized using the room-temperature uniaxial tension tests and three-point bending tests.

During the uniaxial tension tests, the samples were stretched at a strain rate of 2.7%/min. **Figure 3e** and **Figure 3f** show the stress-strain relationships, stiffness, and ultimate strength of the composite laminates under the uniaxial tensile tests. It is shown that after the second-stage heat treatment, the stiffness and strength of composite laminate is increased by 47.7% and 29.3% respectively compared to the laminate before heat processing.

Three-point bending tests were performed on the 3D printed samples before and after the heat treatment, as shown in **Figure 3g.** During the tests, the crosshead speed was 1mm/min as designated by ASTM standard D7264. The span length was 80 mm, and the resulting span-to-thickness ratio was approximately 36:1. The force (P) - displacement (δ) relation was recorded during the tests. The flexural stress at the outer surface mid-span was calculated as $\sigma = 3PL/2bh^2$, with L being the support span length, b being the support span length, and h being the sample thickness. The strain at the outer surface was calculated using $\varepsilon = 6\delta h/L^2$. The relationship between the maximum flexural stress and maximum strain at mid-span of composite samples before and after heat treatment is presented in **Figure 3h**. It is observed that after the heat treatment, the flexural modulus of the composite laminate is increased by 3.1 times (from 526 MPa to 1608 MPa). The strength of the specimen, which is determined by the maximum stress on the stress-strain curve, is enhanced by almost 11 times (from ~2MPa to 23MPa). As previously discussed, the improved mechanical properties of the printed laminate are attributed to the increased matrix stiffness and enhanced bonding between the composite filaments and printing layers after the heat treatment. Another interesting observation is that, at a strain of 0.017, the laminate without heat treatment exhibited a linear V-shaped deformation pattern. This indicates localized stress concentration and deformation in the middle section of the sample, as well as poor stress transfer efficiency within the printed composites. In contrast, the composite laminate after second-stage transesterification shows a more uniform bending deformation along the span. The final failure model of the laminate translated from interlaminar shear failure to laminar tension

failure. This difference highlights the dramatically improved resistance of the printed laminates against bending load after the heat treatment.

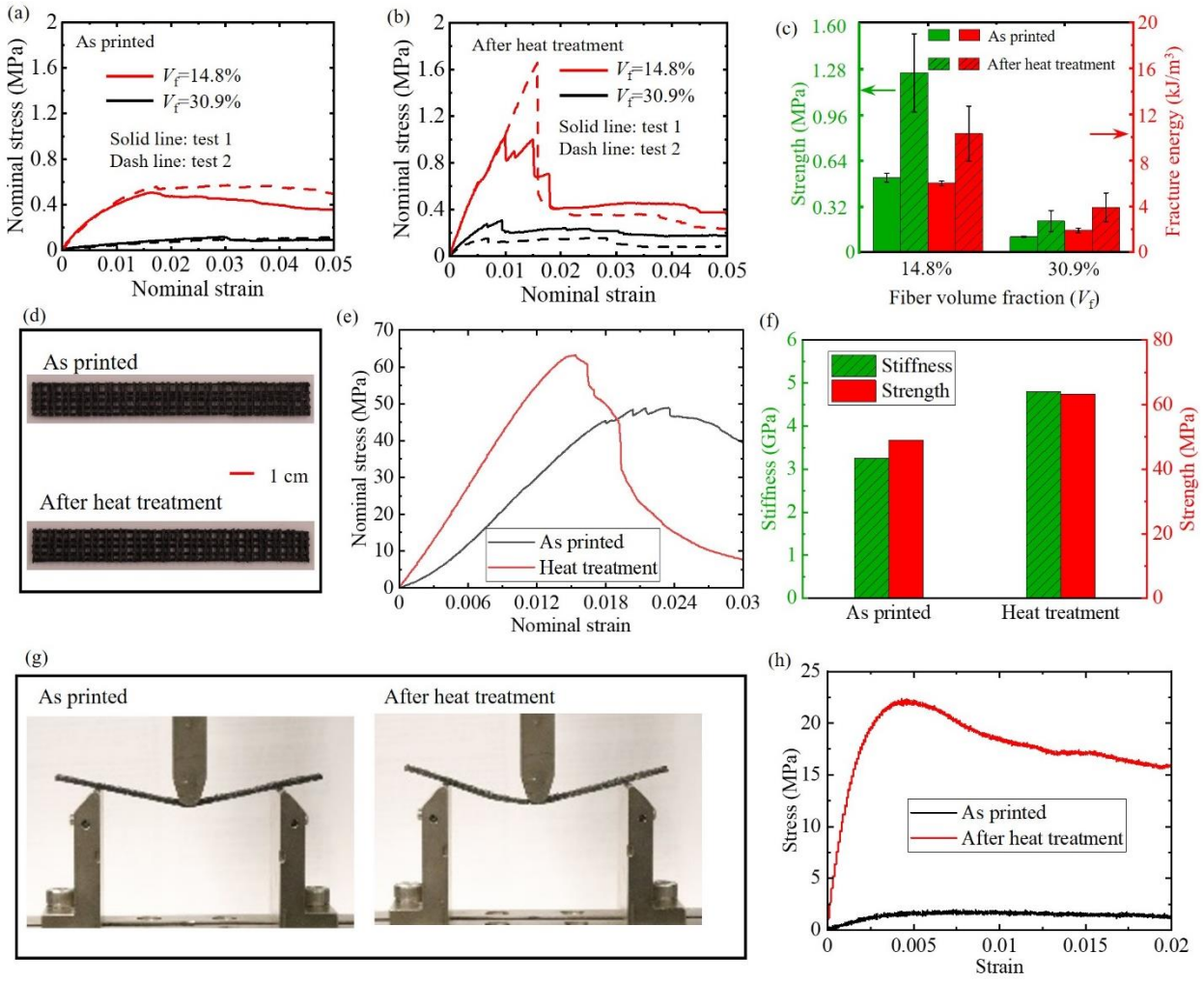

Figure 3. Mechanical performance of lamina samples for transverse loading and the laminate for three-point bending. (a)-(b) Nominal stress-strain of lamina samples with different fiber volume fractions along transverse direction before and after heat treatment. (c) A summary of the ultimate strength and fracture energy of the lamina along transverse direction. (d) Printed laminate samples before and after heat treatment. (e) Tensile stress-strain curve of laminate samples before and after heat treatment. (f) A summary plot of stiffness and strength for laminate samples. (g). Bending deformation of laminate samples before and after heat treatment at the strain of 0.017. (h) Maximum flexural stress as a function of the maximum strain at mid-span of composite samples during the three-point bending tests.

2.3 Repairability, reshapability and recyclability of 3D printed CFRPs

The incorporation of reparability, reshapability, and recyclability to the 3D printed CFRPs offers several benefits for composite rapid prototyping. For example, the composite prototype can be reshaped or repaired onsite without losing their mechanical integrity, which allows the designers and engineers to make necessary adjustments and fine-tune prototypes without the need to print an entirely new part. As a result, it will lead to faster iterations, shorter development cycles, lower cost of prototyping, and more creative freedom in the design process. In addition, the reparability and recyclability of printed composites contribute to a more sustainable approach to prototyping. By minimizing material waste and promoting reusability, they help mitigate the environmental impact associated with rapid prototyping processes.

For conventional 3D printed thermosetting structures, they cannot be repaired after damage because the chemically crosslinked networks are permanently destroyed. In this study, the interfacial welding effect of the adopted two-stage resin enables the repairability of printed composites through thermally activated BERs [67]. To demonstrate the repairability, composite lamina samples were printed with two layers and manually drilled with a circular hole to simulate a mechanical damage. The repair process of the lamina samples involves two steps. First, filaments with the same fiber volume fraction were laid over the damaged area. Subsequently, the entire composite lamina was subject to thermal treatment in an oven. During this process, the thermal treatment not only stiffens the newly deposited composite materials, but also enhances their covalent bonding with the substrate, ensuring a strong and durable repair.

Figure 4a presents the printed composite lamina, a lamina subjected to damage, and two repaired samples. The damaged lamina was manually punched with a circular hole to mimic a damage that is commonly seen in low-velocity impact. For the repair samples, composite filaments were printed onto the surface to cover the damaged area. The newly deposited filaments were oriented either obliquely (Sample A) or in the same direction as the substrate (Sample B). The repairing process resembles the conventional external patch repair process of composite structures. However, the repairing process was entirely automated through the 3D printing process, and there was no manual intervention on the damaged sample, such as trimming, material removal, or surface treatment. After printing new composite layers on the damaged material, the samples are subject to post heating at 160^{o}C for one hour.

Figure 4b the mechanical performance of these samples through uniaxial tensile tests. As expected, the presence of damage results in a reduction of approximately 50% in stiffness and

around 45% in ultimate strength compared to the undamaged composite sample. This decrease can be attributed to significant stress concentrations around the hole, which promotes cracking during uniaxial tension. However, both repaired Sample A and repaired Sample B exhibit impressive recoveries in mechanical properties. Specifically, repaired Sample A recovers approximately 60% of the stiffness and around 82% of the ultimate strength, while repaired Sample B achieves an even better recovery, with roughly 85% of the stiffness and 93% of the ultimate strength being regained. This substantial improvement in mechanical properties can be attributed to two key factors. Firstly, the newly added composite layer, especially after the thermal treatment, exhibits high mechanical stiffness and strength, which provides additional support and enhances the overall load-bearing capabilities of the repaired composite. Secondly, the interfacial welding effect of the matrix material during the thermal treatment facilitates efficient load transfer between the parent material and the newly added composite layer.

The mechanical performance of the repaired composites is closer to that of the original printed composites when the newly added materials are printed in the same orientation as the substrate. Nevertheless, it is important to acknowledge that achieving a full recovery of stiffness and strength in printed composites is challenging due to the discontinuity of fiber reinforcements around the repaired domain, which can lead to a degradation in the mechanical behavior of the composite lamina.

Figure 4c demonstrates the bending stiffness of the printed CFRPs after damage repair. The four lamina samples were placed between two supports and subjected to fixed weights of 100 g at the middle point. Under the three-point bending loading condition, a lower deflection indicates a higher flexural stiffness of the composite samples. As shown in the figure, the damaged sample displays a notable deflection of 7.12 mm. After repair, Sample A exhibits a decreased deflection of 6.20 mm, and the Sample B shows a minimal deflection (1.58 mm) comparable to that of the control sample (1.06 mm) without any prior damage. By considering that bending deflection is directly proportional to beam stiffness, it can be estimated that the stiffness of the repaired composites has been improved by 4.5 times compared to their state prior to repair.

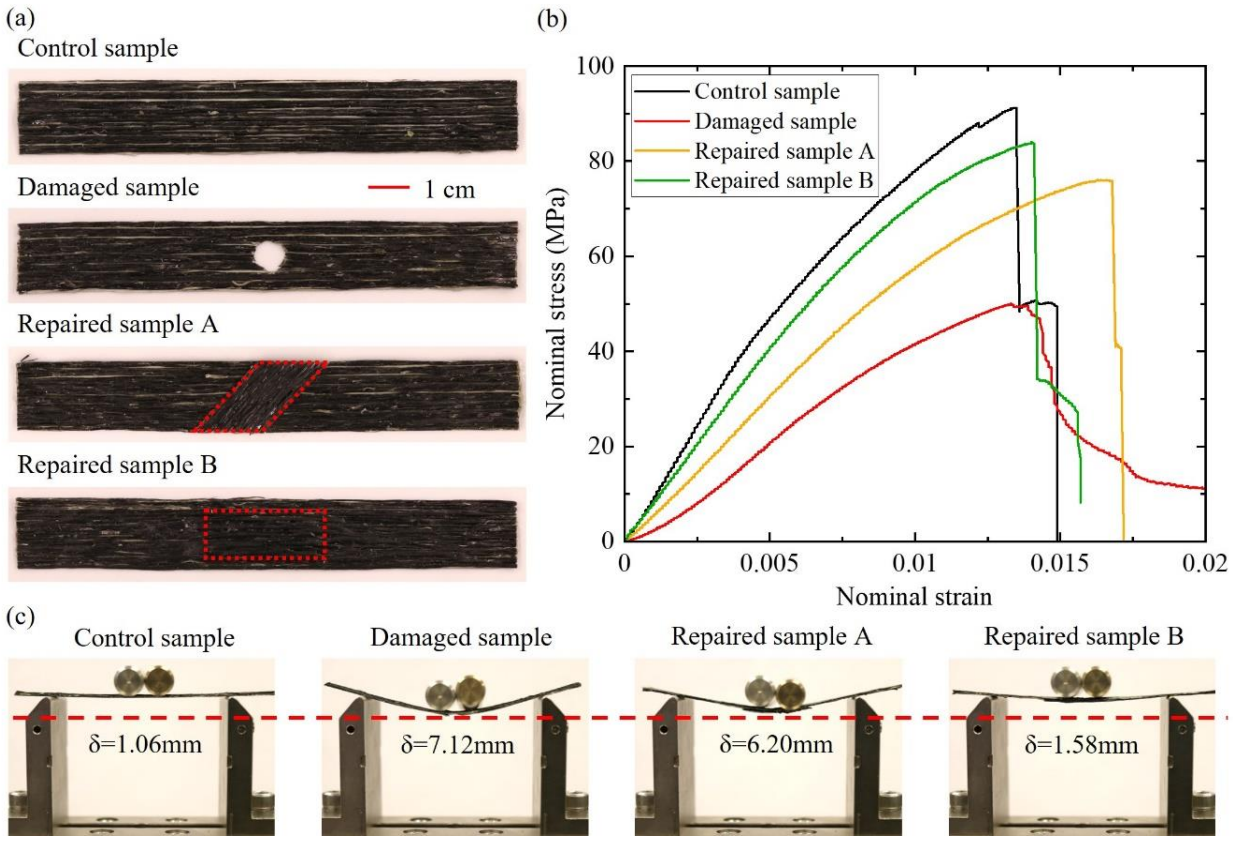

Figure 4. Repairability of the 3D printed CFRPs. (a) The appearances of the printed lamina sample without damage, the damaged sample, and the repaired samples with filaments deposited in different directions. (b) The nominal stress-strain curves of the different composite samples. (c) Bending demonstration of the different composite samples.

Polymer networks with the capability of bond exchange reactions (BERs) have shown to exhibit malleability at high temperatures for the shape reformatting and reprocessing [46, 74]. This malleability is attributed to the effective stress relaxation that occurs during the chain cleavage of BERs. In this study, we extend the malleability capabilities of the matrix to reshape 3D printed CFRPs.

To demonstrate this concept, we printed composite lamina and 0/90˚ symmetric laminate with 14.8% fiber volume fraction. The monomer-to-cross linker weight ratio was slightly increased from 1:0.5 to 1:0.72 to better handle the printable resin. The samples were then sandwiched between molds or mounted on a substrate for shape reforming. Subsequently, they were heated in an oven at 160˚ for one hour, while a moderate force was applied to hold the desired shape during the reforming process. **Figure 5a**, **Figure 5b** and **Figure 5c** respectively showcase the 3D printed

composite lamina and laminate reformed into wave-shaped lamina, helix-shaped lamina, and dome-shaped laminate. It is important to note that the shape reforming of printed composite specimens is permanent as a result of the BER-induced stress relaxation, which is different from the conventional viscoelastic behavior observed in glassy polymers. Further heating the reformed composite structures in a free-standing state did not result in any additional shape changes. The demonstrations suggest that the 3D printed CFRPs exhibit excellent reshapability, which allows the efficient fabrication of complex 3D composite structures from 2D laminates without the need for intricate molding, complex motion control, and pathway planning required in 3D spatial printing.

The adoption of the two-stage UV curable resin also enables the recyclability of 3D printed CFRPs. As illustrated in **Figure S4** of the **Supplementary Materials**, the thermoset matrix with ester bonds on the chain backbone can be fully depolymerized after immersing in the ethylene glycol (EG) solvent at high temperatures [53, 75-79]. During this process, the small solvent molecules diffuse into the network and gradually break the polymer chains into oligomers. The clean fiber can be reclaimed without notable damage.

Figure 5d demonstrates the recycling process of the 3D printed CFRPs. Composite filaments with 14.8% fiber volume fractions were printed and placed in a glassware container filled with EG solvent. 2wt% TBD catalyst was also added into the solvent to facilitate the transesterification BERs. After heating in an oven at 160 ˚C for one hour, the thermoset matrix was fully depolymerized. The microscopic images in the **Supplementary Materials** (**Figure S5**) confirm that the reclaimed fibers are clean, devoid of any damage or residual resin. The reclaimed fiber was then dried for 30 minutes and fed into the syringe to print a fractal-shaped composite sample. This process can be repeated to print another composite lamina sample using the same fiber bundle.

It is noted that the depolymerization process of the thermoset matrix is fully reversible. The polymer solution can be repolymerized to form a near-identical thermoset network by heating it in an open environment to evaporate excessive EG solvent [80]. Therefore, they can be potentially reused for the subsequent rounds of composite printing after careful adjustment of the resin viscosity and post-curing conditions. In this study, we primarily focus on the recycling of the continuous fiber bundle, which is the most valuable component of the composites.

In addition to processing temperature and time, the repair, reshaping, and recycling capabilities of printed thermosetting composites are influenced by the density of the initial irreversible covalent

bonds (black dots in Figure 1b). Firstly, the ability to reshape and repair these composites relies on the BER-induced stress relaxation and the interfacial welding effect of the matrix material. If the mole ratio of the acrylate crosslinker within the printable resin is increased, it results in a higher density of irreversible crosslinking sites. This, in turn, reduces the flexibility of polymer chains and slows down the kinetics of BER. Consequently, a higher temperature or longer processing time is required to achieve an equivalent degree of stress relaxation and interfacial welding [74, 81-83]. Secondly, a higher initial crosslinking density within the network leads to reduced free volume among polymer chains and, consequently, lower solvent diffusivity. This, in turn, results in a slower depolymerization process of the matrix material during recycling. To fully recycle the 3D printed composite under these conditions, higher temperatures or an increased amount of catalyst may be necessary [84, 85]. Despite the potential influences, it is important to note that this study utilized an identical resin recipe for all characterizations. Therefore, the impact of irreversible bond density is consistent throughout the study.

In addition to the adopted two-stage resin with continuous carbon fiber bundle, in the **Supplementary Materials** (Section S7), we extend the strategy to include another acrylate/epoxy-based two-stage UV-curable resin and another polyester-based continuous fiber. The polyester fiber thread was purchased from Coats & Clark Inc. (Charlotte, NC, USA). The acrylate/epoxy two-stage resin was prepared following the previous work by Kuang et al. [86]. Utilizing the DIW method, two sets of composite samples were printed using the acrylate/epoxy two-stage resin, embedded with 14.8% continuous carbon fiber and polyester fiber, respectively. During the second-stage thermal treatment, an interpenetrating network formed between the epoxy and acrylate species, which contributed to fixing the new configuration of the composite lamina during the shape reforming process (**Figure S7**). Because the cured acrylate/epoxy two-stage network contains ester bonds in the chain backbone, it can be entirely depolymerized using EG solvent mixed to recover the embedded carbon fiber bundle (**Figure S8**). These supplementary tests confirm that the strategy can be applied to other two-stage resins and continuous fibers.

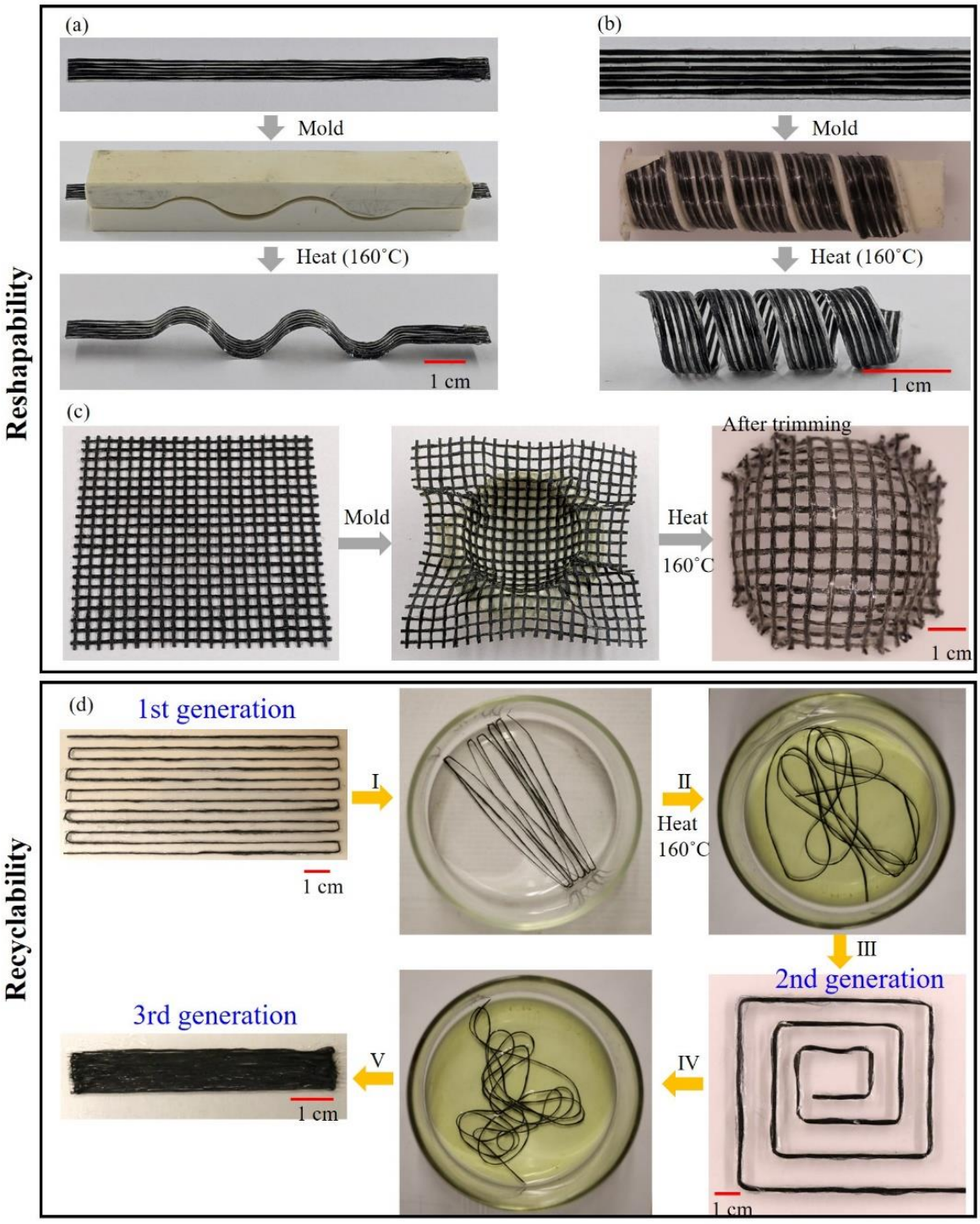

Figure 5. Reshapability and recyclability of the 3D printed CFRPs with two-stage curable resin. The printed 2D composite samples are shown to be reshaped to (a) wave-shaped lamina, (b) helix-shaped lamina, and (c) dome-shaped laminate after heating at 160 ˚C for an hour. (d) Demonstration of the recyclability: step I, the printed 1st generation filament was placed into the glassware with EG solvent; step II, the glassware was heated an oven at 160 ˚C for an hour. The matrix material was fully depolymerized; step III, the fiber

bundle was reclaimed and fed into the printer to print 2nd generation fractal-shaped sample; step IV, the depolymerization process was repeated; step V, the same fiber bundle was recovered and used to print another lamina sample.

3. Conclusion

In this study, we present the potential of the two-stage UV curable resin as a promising material candidate for addressing significant challenges in the current 3D printing of continuous fiber composites.

First, during the thermal treatment, the second-stage polymerization increases the matrix crosslinking density through bond exchange reactions (BERs) and substantially boosts its modulus by ~11 times. Additionally, the BERs enable the surface welding effect among adjacent filaments and printing layers, leading to their robust covalent bonding at the interfaces. These two mechanisms greatly improve the overall mechanical properties of the printed composites. As notable results, after thermal treatment, the composite lamina with 30.9% carbon fiber experiences a remarkable 101% increase in transverse modulus and a 103% increase in transverse strength. Furthermore, the flexural stiffness and strength of the composite laminate under three-point bending are enhanced by factors of 3.1 and 11, respectively.

Second, the interfacial welding effect of the two-stage curable resins enables the repair of 3D printed composites and allows for the recovery of most mechanical properties., which is a desirable feature to enhance the durability and reliability of composite products. Due to the BER-induced stress relaxation in the thermoset matrix, the 3D printed composites become malleable at high temperatures and can be reshaped into new configurations through simple heating. Consequently, complex 3D composite structures can be efficiently fabricated from 2D laminates without the need for complex motion control or pathway planning. Finally, the 3D printed composites with the two-stage UV curable resin are fully recyclable, wherein the embedded continuous carbon fiber can be reclaimed for the subsequent printing. The recyclability contributes to minimizing the manufacturing cost and mitigating the generation of hazard waste.

It is important to note that a wide range of two-stage UV-curable resins have already been developed and are commercially available. The fundamental understanding gained from this study has the potential to be extended to other types of resins with different molecular mechanisms, including those with different BER chemistry or hybrid resins with dual networks.

4. Materials and Experiments

4.1 Material preparation

The UV-curable resin was prepared using commercially available chemicals from Sigma-Aldrich (St. Louis, MO). The formulation included the monomer 2-hydroxy-3-phenoxypropyl acrylate, the crosslinker biphenol A glycerolate diacrylate, the photo initiator phenylbis (2,4,6-trimethylbenzoyl) phosphine oxide, and the BER catalyst triazabicyclodecene. The chemical structures of these ingredients are illustrated in **Figure 1a**. To prepare the resin, the biphenol A glycerolate diacrylate was initially heated in an oven at 70 ˚C for 10 min to reduce its viscosity. Subsequently, 20g of 2-hydroxy-3-phenoxypropyl acrylate and 10g of biphenol A glycerolate diacrylate were added to a 70 ml glass vial. 2% of phenylbis (2,4,6-trimethylbenzoyl) phosphine oxide and 2% of triazabicyclodecene were added to the solution. The entire solution was then placed in the oven at 70 ˚C for an additional 10 min, while a vortex mixer was used to thoroughly mix the solution.

4.2 Direct ink writing 3D printing

The adopted DIW setup for the 3D printing of CFRPs is schematically shown in the **Supplementary Materials, Figure S2**. The print head comprises a syringe barrel, a feeding tube, a printing nozzle, and UV light sources. The syringe stores the solution as printable ink and is securely attached to the motion stage using adapters. A tube is concentrically attached to the syringe to guide the feeding of continuous fiber. The fiber interacts with the ink at the end of the feeding tube. A straight dispensing needle is attached to the syringe and used as printing nozzle. To prevent resin curing around the needle tip and avoid nozzle clogging, a rubber cap (~2mm diameter) is placed at the tip of the needle to block the UV light, which is shown to be effective to print composites along straight or curved pathways. The design of the printer head is independent of the machine dynamics, allowing for easy mounting on most commercially available motion stages. In this study, a motion stage of a commercial FDM printer (Makerfarm Prusa i3y) is employed to control the movement of the printer head. The motion stage is controlled from a desktop computer using user-defined G-codes as motion commands. After filament deposition, the matrix resin rapidly solidifies upon UV irradiation (405nm, 100mW) and adheres to the print bed, which exerts pulling forces onto the resin-infused fiber as the needle continues to move.

4.3 Material characterizations

An MTS tester (MTS Criterion Model 41, MTS systems Corp., Eden Prairie, MN, USA) was used to test the mechanical behavior at room temperature. To ensure secure clamping of the samples, all printed filaments, lamina, and laminate were cured onto specifically designed specimen holders (see the **Supplementary Materials**, **Figure S3** for examples). The samples were tested using the MTS machine with a loading rate of 3mm/min. The glass transition behaviors of the UV cured resin were characterized using a dynamic mechanical analysis (DMA) tester (Model Q800, TA Instruments, New Castle, DE, USA). The analysis was performed at a frequency of 1Hz and a strain level of 0.15%. The temperature was first equilibrated at -10˚C for 5 min, and then increased at a heating rate of 1˚C/min. The glass transition temperature (Tg) was determined as the temperature corresponding to the peak of the tan δ curve.

Author Contributions

Huan Jiang: Investigation, Formal Analysis, Visualization, Writing – original draft; **Arif M. Abdullah**: Investigation, Formal Analysis, Visualization; **Yuchen Ding**: Investigation, Validation; **Christopher Chung**: Investigation, Validation; **Martin Dunn**: Supervision, Writing – review & editing, Project administration, Funding acquisition; **Kai Yu**: Conceptualization, Supervision, Writing – review & editing, Project administration, Funding acquisition

Conflicts of Interest

There are no conflicts to declare

Acknowledgement

K.Y. and M.D. acknowledge the support of AFOSR grant (FA-20-1-0306; Dr. B.-L. “Les” Lee, Program Manager). K.Y. acknowledges the support from the National Science Foundation (grant CMMI-1901807).

References

1. D. D. Chung, *Carbon composites: composites with carbon fibers, nanofibers, and nanotubes*, Butterworth-Heinemann, 2016.
2. P. Morgan, *Carbon fibers and their composites*, CRC press, 2005.
3. Z. C. Eckel, C. Zhou, J. H. Martin, A. J. Jacobsen, W. B. Carter and T. A. Schaedler, *Science*, 2016, **351**, 58-62.

4. M. Zarek, M. Layani, I. Cooperstein, E. Sachyani, D. Cohn and S. Magdassi, *Advanced Materials*, 2016, **28**, 4449-4454.
5. Q. Ge, A. H. Sakhaei, H. Lee, C. K. Dunn, N. X. Fang and M. L. Dunn, *Scientific Reports*, 2016, **6**, 31110.
6. J. R. Tumbleston, D. Shirvanyants, N. Ermoshkin, R. Janusziewicz, A. R. Johnson, D. Kelly, K. Chen, R. Pinschmidt, J. P. Rolland, A. Ermoshkin, E. T. Samulski and J. M. DeSimone, *Science*, 2015, **347**, 1349-1352.
7. Q. Ge, H. J. Qi and M. Dunn, *Applied Physics Letters*, 2013, **103**, 131901-131901.
8. Y. Mao, K. Yu, M. S. Isakov, J. Wu, M. L. Dunn and H. Jerry Qi, *Scientific Reports*, 2015, **5**, 13616.
9. F. Van Der Klift, Y. Koga, A. Todoroki, M. Ueda, Y. Hirano and R. Matsuzaki, *Open Journal of Composite Materials*, 2016, **6**, 18.
10. K.-i. Mori, T. Maeno and Y. Nakagawa, *Procedia Engineering*, 2014, **81**, 1595-1600.
11. R. Matsuzaki, M. Ueda, M. Namiki, T.-K. Jeong, H. Asahara, K. Horiguchi, T. Nakamura, A. Todoroki and Y. Hirano, *Scientific Reports*, 2016, **6**, 23058.
12. N. Li, Y. Li and S. Liu, *Journal of Materials Processing Technology*, 2016, **238**, 218-225.
13. C. Yang, X. Tian, T. Liu and Y. Cao, *Rapid Prototyping Journal*, 2017, **23**, 209-215.
14. X. Tian, T. Liu, C. Yang, Q. Wang and D. Li, *Composites Part A: Applied Science and Manufacturing*, 2016, **88**, 198-205.
15. X. Tian, T. Liu, Q. Wang, A. Dilmurat, D. Li and G. Ziegmann, *Journal of Cleaner Production*, 2017, **142**, 1609-1618.
16. G. D. Goh, V. Dikshit, A. P. Nagalingam, G. L. Goh, S. Agarwala, S. L. Sing, J. Wei and W. Y. Yeong, *Materials & Design*, 2018, **137**, 79-89.
17. D. Jiang and D. Smith, 2016.
18. T. D. Ngo, A. Kashani, G. Imbalzano, K. T. Q. Nguyen and D. Hui, *Composites Part B: Engineering*, 2018, **143**, 172-196.
19. B. Bhushan and M. Caspers, *Microsystem Technologies*, 2017, **23**.
20. M. Mao, J. He, X. Li, B. Zhang, Q. Lei, Y. Liu and D. Li, *Journal*, 2017, **8**.
21. H. Chen, Y. Hu, C. Luo, Z. Lei, S. Huang, J. Wu, Y. Jin, K. Yu and W. Zhang, *Journal of the American Chemical Society*, 2023, **145**, 9112-9117.
22. W. Hao, Y. Liu, H. Zhou, H. Chen and D. Fang, *Polymer Testing*, 2018, **65**, 29-34.
23. Y. Ming, S. Zhang, W. Han, B. Wang, Y. Duan and H. Xiao, *Additive Manufacturing*, 2020, **33**, 101184.
24. X. He, Y. Ding, Z. Lei, S. Welch, W. Zhang, M. Dunn and K. Yu, *Additive Manufacturing*, 2021, **40**, 101921.
25. K. Tyler, *US patent*, 2014.
26. A. M. Abdullah, Y. Ding, X. He, M. Dunn and K. Yu, *Journal of Composite Materials*, 2022, **57**, 851-863.
27. M. A. Rahman, M. Z. Islam, L. Gibbon, C. A. Ulven and J. J. La Scala, *Polymer Composites*, 2021, **42**, 5859-5868.
28. M. Invernizzi, G. Natale, M. Levi, S. Turri and G. Griffini, *Materials (Basel)*, 2016, **9**.
29. R. Zou, Y. Xia, S. Liu, P. Hu, W. Hou, Q. Hu and C. Shan, *Composites Part B: Engineering*, 2016, **99**, 506-513.
30. S.-H. Ahn, S. And, P. Wright, M. Montero, D. Odell and S. Roundy, *Rapid Prototyping Journal*, 2002, **8**.

31. Q. Sun, G. Rizvi, C. T. Bellehumeur and P. Gu, *Rapid Prototyping Journal*, 2008, **14**, 72-80.
32. I. G. Ian Gibson, *Journal*, 2015.
33. X. Chen, L. Li, T. Wei, D. C. Venerus and J. M. Torkelson, *ACS Applied Materials & Interfaces*, 2019, **11**, 2398-2407.
34. X. He, X. Shi, C. Chung, Z. Lei, W. Zhang and K. Yu, *Composites Part B: Engineering*, 2021, **221**, 109004.
35. J. R. Duflou, J. De Moor, I. Verpoest and W. Dewulf, *CIRP Annals*, 2009, **58**, 9-12.
36. S.-i. Sakai, H. Yoshida, J. Hiratsuka, C. Vandecasteele, R. Kohlmeyer, V. S. Rotter, F. Passarini, A. Santini, M. Peeler, J. Li, G.-J. Oh, N. K. Chi, L. Bastian, S. Moore, N. Kajiwara, H. Takigami, T. Itai, S. Takahashi, S. Tanabe, K. Tomoda, T. Hirakawa, Y. Hirai, M. Asari and J. Yano, *Journal of Material Cycles and Waste Management*, 2014, **16**, 1-20.
37. A. Santini, L. Morselli, F. Passarini, I. Vassura, S. Di Carlo and F. Bonino, *Waste Management*, 2011, **31**, 489-494.
38. J. Cui and E. Forssberg, *Journal of Hazardous Materials*, 2003, **99**, 243-263.
39. Z. Lei, H. Chen, C. Luo, Y. Rong, Y. Hu, Y. Jin, R. Long, K. Yu and W. Zhang, *Nature Chemistry*, 2022, **14**, 1399-1404.
40. X. Huang, B. Zhou, G. Sun, X. Yang, Y. Wang and X. Zhang, *Nano Energy*, 2023, **116**, 108843.
41. H.-X. Chen, Z.-P. Lei, S.-F. Huang, H. Jiang, K. Yu, Y.-H. Jin and W. Zhang, *Chinese Journal of Polymer Science*, 2023, 1-7.
42. K. Yu, H. J. Qi, P. Taynton, W. Zhang and M. L. Dunn, 2014.
43. P. Taynton, H. Ni, C. Zhu, K. Yu, S. Loob, Y. Jin, H. J. Qi and W. Zhang, *Advanced Materials*, 2016, **28**, 2904-2909.
44. X. He, Z. Lei, W. Zhang and K. Yu, *3D Printing and Additive Manufacturing*, 2019, **6**, 31-39.
45. X. Kuang, Z. Zhao, K. Chen, D. Fang, G. Kang and H. J. Qi, *Macromolecular Rapid Communications*, 2018, **39**, 1700809.
46. C. Luo, B. Zhang, W. Zhang, C. Yuan, M. Dunn, Q. Ge and K. Yu, *Journal of the Mechanics and Physics of Solids*, 2019, **126**, 168-186.
47. D. P. Nair, N. B. Cramer, J. C. Gaipa, M. K. McBride, E. M. Matherly, R. R. McLeod, R. Shandas and C. N. Bowman, *Advanced Functional Materials*, 2012, **22**, 1502-1510.
48. B. Zhang, A. Serjouei, Y.-F. Zhang, J. Wu, H. Li, D. Wang, H. Y. Low and Q. Ge, *Chemical Engineering Journal*, 2021, **411**, 128466.
49. X. Fernández-Francos, O. Konuray, X. Ramis, À. Serra and S. De la Flor, *Journal*, 2021, **14**.
50. O. Konuray, X. Fernández-Francos, X. Ramis and À. Serra, *Journal*, 2018, **10**.
51. K. Yu, Q. Shi, M. L. Dunn, T. Wang and H. J. Qi, *Advanced Functional Materials*, 2016, **26**, 6098-6106.
52. C. Luo, Z. Lei, Y. Mao, X. Shi, W. Zhang and K. Yu, *Macromolecules*, 2018, **51**, 9825-9838.
53. K. Yu, H. Yang, B. H. Dao, Q. Shi and C. M. Yakacki, *Journal of the Mechanics and Physics of Solids*, 2017, **109**, 78-94.
54. D. Montarnal, M. Capelot, F. Tournilhac and L. Leibler, *Science*, 2011, **334**, 965-968.

55. P. Taynton, K. Yu, R. K. Shoemaker, Y. Jin, H. J. Qi and W. Zhang, *Advanced Materials*, 2014, **26**, 3938-3942.
56. X. Shi, Q. Ge, H. Lu and K. Yu, *Soft Matter*, 2021, **17**, 2104-2119.
57. D. W. Hanzon, N. A. Traugutt, M. K. McBride, C. N. Bowman, C. M. Yakacki and K. Yu, *Soft Matter*, 2018, **14**, 951-960.
58. J. A. Lewis, *Advanced Functional Materials*, 2006, **16**, 2193-2204.
59. J. A. Lewis and G. M. Gratson, *Materials Today*, 2004, **7**, 32-39.
60. G. M. Gratson, M. Xu and J. A. Lewis, *Nature*, 2004, **428**, 386.
61. C. P. Ambulo, J. J. Burroughs, J. M. Boothby, H. Kim, M. R. Shankar and T. H. Ware, *ACS Applied Materials & Interfaces*, 2017, **9**, 37332-37339.
62. A. Kotikian, R. L. Truby, J. W. Boley, T. J. White and J. A. Lewis, *Advanced Materials*, 2018, **30**, 1706164.
63. V. Rohatgi, A. Adur, K. Shih, M. Botros, R. Previty and G. Castle, *Journal*, 2003.
64. J. Frketic, T. Dickens and S. Ramakrishnan, *Additive Manufacturing*, 2017, **14**, 69-86.
65. B. T. Astrom, *Manufacturing of polymer composites*, CRC press, 1997.
66. D. A. Papargyris, R. J. Day, A. Nesbitt and D. Bakavos, *Composites Science and Technology*, 2008, **68**, 1854-1861.
67. B. Zhang, K. Kowsari, A. Serjouei, M. L. Dunn and Q. Ge, *Nature Communications*, 2018, **9**, 1831.
68. J. L. Gómez Ribelles, M. M. Pradas, J. M. M. Dueñas and C. T. Cabanilles, *Journal of Non-Crystalline Solids*, 2002, **307-310**, 731-737.
69. M. Zhao, L. Meng, L. Ma, L. Ma, X. Yang, Y. Huang, J. E. Ryu, A. Shankar, T. Li and C. Yan, *Composites Science and Technology*, 2018, **154**, 28-36.
70. R. Zhang, B. Gao, Q. Ma, J. Zhang, H. Cui and L. Liu, *Materials & Design*, 2016, **93**, 364-369.
71. O. A. Panina, A. S. Nemov, A. Y. Zobacheva, I. A. Kobykhno, O. V. Tolochko and V. K. Yadykin, *Materials Today: Proceedings*, 2020, **30**, 559-563.
72. D. Mamalis, T. Flanagan and C. M. Ó Brádaigh, *Composites Part A: Applied Science and Manufacturing*, 2018, **110**, 93-105.
73. X. He, D. W. Hanzon and K. Yu, *J Polym Sci Pol Phys*, 2018, **56**, 402-413.
74. K. Yu, Q. Shi, H. Li, J. Jabour, H. Yang, M. Dunn, T. Wang and H. Qi, *Journal of the Mechanics and Physics of Solids*, 2016, **94**, 1-17.
75. K. Yu, Q. Shi, M. L. Dunn, T. J. Wang and H. J. Qi, *Advanced Functional Materials*, 2016, **26**, 6098-6106.
76. Q. Shi, K. Yu, X. Kuang, X. Mu, C. K. Dunn, M. L. Dunn, T. Wang and H. J. Qi, *Materials Horizons*, 2017, **4**, 598-607.
77. X. Shi, D. Soule, Q. Ge, H. Lu and K. Yu, *Materials Today Sustainability*, 2022, **19**, 100167.
78. X. He, Y. Lin, Y. Ding, A. M. Abdullah, Z. Lei, Y. Han, X. Shi, W. Zhang and K. Yu, *International Journal of Extreme Manufacturing*, 2021, **4**, 015301.
79. X. Shi, C. Luo, H. Lu and K. Yu, *Polymer Engineering & Science*, 2019, **59**, E111-E119.
80. X. Shi, D. Soule, Y. Mao, C. Yakacki, H. Lu and K. Yu, *Journal of the Mechanics and Physics of Solids*, 2020, 103918.
81. X. Shi, C. Luo, H. Lu and K. Yu, *Surfaces and Interfaces*, 2021, **26**, 101368.
82. K. Yu, P. Taynton, W. Zhang, M. L. Dunn and H. J. Qi, *Rsc Advances*, 2014, **4**, 48682-48690.

83. K. Yu, P. Taynton, W. Zhang, M. L. Dunn and H. J. Qi, *RSC advances*, 2014, **4**, 10108-10117.
84. C. Luo, C. Chung and K. Yu, *Materials Today Sustainability*, 2023, **23**, 100452.
85. X. Shi, X. He, C. Luo, C. Chung, Y. Ding and K. Yu, *Polymer*, 2022, **252**, 124964.
86. X. Kuang, Z. Zhao, K. J. Chen, D. N. Fang, G. Z. Kang and H. J. Qi, *Macromolecular Rapid Communications*, 2018, **39**.